Imaging Orbital Vortex Lines in Three-Dimensional Momentum Space

T. Figgemeier,[1,*] M. Ünzelmann,[1,*,†] P. Eck,[2,*] J. Schusser,[1,3] L. Crippa,[2] J. N. Neu,[4,5] B. Geldiyev,[1] P. Kagerer,[1] J. Buck,[6,7] M. Kalläne,[6,7] M. Hoesch,[8] K. Rossnagel,[6–8] T. Siegrist,[4,5] L.-K. Lim,[9] R. Moessner,[10] G. Sangiovanni,[2] D. Di Sante,[11] F. Reinert,[1] and H. Bentmann[1,12]

[1]*Experimentelle Physik VII and Würzburg-Dresden Cluster of Excellence ct.qmat, Universität Würzburg, Am Hubland, D-97074 Würzburg, Germany*
[2]*ITPA and Würzburg-Dresden Cluster of Excellence ct.qmat, Universität Würzburg, Am Hubland, D-97074 Würzburg, Germany*
[3]*New Technologies-Research Center, University of West Bohemia, 30614, Pilsen, Czech Republic*
[4]*Department of Chemical and Biomedical Engineering, FAMU-FSU College of Engineering, Tallahassee, Florida 32310, USA*
[5]*National High Magnetic Field Laboratory, Tallahassee, Florida 32310, USA*
[6]*Institut für Experimentelle und Angewandte Physik, Christian-Albrechts-Universität zu Kiel, D-24098 Kiel, Germany*
[7]*Ruprecht Haensel Laboratory, Kiel University and DESY, D-24098 Kiel and D-22607 Hamburg, Germany*
[8]*Deutsches Elektronen-Synchrotron DESY, D-22607 Hamburg, Germany*
[9]*Zhejiang Institute of Modern Physics, Department of Physics, Zhejiang University, Hangzhou, Zhejiang 310027, People's Republic of China*
[10]*Max Planck Institute for the Physics of Complex Systems and Würzburg-Dresden Cluster of Excellence ct.qmat, Noethnitzer Strasse 38, D-01187 Dresden, Germany*
[11]*Department of Physics and Astronomy, University of Bologna, I-40127 Bologna, Italy*
[12]*Center for Quantum Spintronics, Department of Physics, NTNU Norwegian University of Science and Technology, NO-7491 Trondheim, Norway*

(Received 30 April 2024; revised 10 October 2024; accepted 2 January 2025; published 13 February 2025)

We report the experimental discovery of orbital vortex lines in the three-dimensional (3D) band structure of a topological semimetal. Combining linear and circular dichroism in soft x-ray angle-resolved photoemission (SX-ARPES) with first-principles theory, we image the winding of atomic orbital angular momentum, thereby revealing—and determining the location of—lines of vorticity in full 3D momentum space. We determine the core of the orbital angular momentum vortex to host an almost movable, twofold, spin-degenerate Weyl nodal line, a topological feature predicted to occur in certain nonsymmorphic crystals. These results establish bimodal dichroism in SX-ARPES as a robust approach to trace 3D orbital textures. Our findings constitute the first imaging of nontrivial quantum-phase winding at line nodes and may pave the way to new orbitronic phenomena in quantum materials.

DOI: 10.1103/PhysRevX.15.011032 Subject Areas: Condensed Matter Physics

I. INTRODUCTION

The geometric structure of Bloch wave functions in a periodic lattice may host nontrivial textures in momentum space underpinning the unique properties of topological quantum matter [1–15]. Topological textures at pointlike band degeneracies have been extensively studied in both two- and three-dimensional systems. Important examples include spin-momentum-locked Dirac surface states in topological insulators [16], Dirac nodes in graphene [17], and Berry-flux monopoles in Weyl semimetals [18–20] and in chiral topological semimetals [21–24]. In contrast, higher-dimensional wave-function textures, such as line vortices, have not been observed experimentally so far. Given the importance of vortices in real space—particularly prominent in superfluids [25], superconductors [26], and, indeed, the early Universe [27,28]—it may seem surprising that line vortices in reciprocal space have thus far entirely eluded detection, despite the fact that their possible existence is theoretically firmly established: Pseudospin vortex rings have recently been predicted to emerge at nodal line degeneracies in 3D topological

*These authors contributed equally to this work.
†Contact author: muenzelmann@physik.uni-wuerzburg.de

Published by the American Physical Society under the terms of the Creative Commons Attribution 4.0 International license. Further distribution of this work must maintain attribution to the author(s) and the published article's title, journal citation, and DOI.

semimetals [25,29], and they may result in topological quantum transport properties [30–32]. More broadly, being associated with phenomena such as (Berry) flux quantization and quantum phase winding, momentum space vortex lines are, in some respects, analogous to magnetic vortices in type-II superconductors, a central paradigm in condensed matter physics.

The fact that their observation has so far remained elusive is presumably partly due to two reasons. First, it remains unclear how pseudospin winding at line nodes [25,29] reflects in spectroscopically accessible quantum degrees of freedom. Second, imaging vorticity across extended volumes of 3D k-space is experimentally challenging, requiring a complete 3D map of the wave-function properties, which we have now achieved with the necessary phase-sensitive and momentum-resolved contrast via linear and circular dichroism in soft x-ray angle-resolved photoelectron spectroscopy (SX-ARPES) [20,22,23,33,34]. Our central result is a 3D map of reciprocal space that unambiguously exhibits topological vortex lines in the orbital texture of TaAs. In recent years, this compound has attracted broad attention, especially for hosting Weyl points [18–20,35–37]. However, the topological features exposed in this work are entirely distinct from the previously discussed (Weyl point) physics. In particular, we have now detected line vortices of orbital angular momentum (OAM) that manifest a new class of Weyl nodal lines [38] pinned to the vortex cores. The OAM has recently attracted broad attention in condensed matter physics, particularly with regard to its use as a quantum degree of freedom to accomplish orbital analogs of spintronic phenomena. Our work may therefore put topological nodal line semimetals in the spotlight of orbitronics [39–41].

In the following, we first analyze the band dispersion around a twofold spin-degenerate band crossing using SX-ARPES and density functional theory (DFT) bulk band structure calculations. The focus then shifts to the properties of the wave functions of the corresponding eigenstates. More precisely, we investigate the 3D momentum dependence of the atomic OAM using dichroic SX-ARPES supported by state-of-the-art simulations of the photoemission intensity, DFT, and an effective minimal model. Finally, we utilize dichroism under systematically varied experimental parameters to achieve a full vectorial tomography of the orbital vortex texture. Our SX-ARPES experiments have been conducted using the ASPHERE III endstation at the Variable Polarization XUV Beamline P04 of the PETRA III storage ring at DESY (Hamburg, Germany). More details on the experimental and theoretical methods are given in the Appendix.

II. RESULTS

A. Band structure and Weyl nodal line

Figure 1(b) displays SX-ARPES data along ΓΣ obtained at $h\nu = 618$ eV, demonstrating excellent agreement with

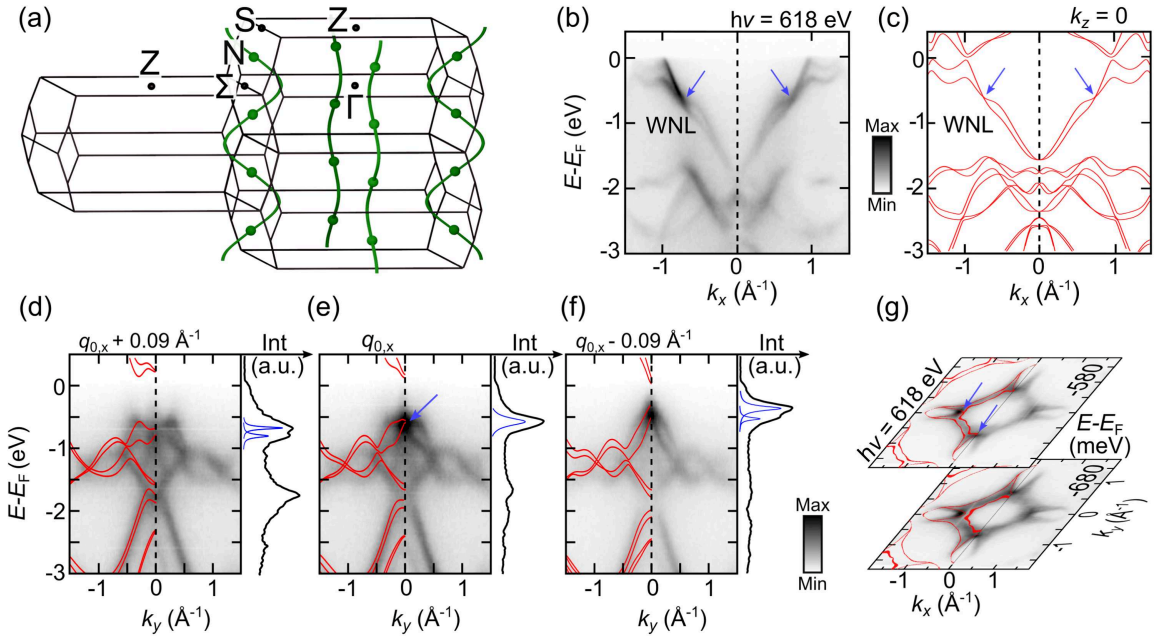

FIG. 1. Almost movable Weyl nodal line in TaAs. (a) Sketch of the TaAs Brillouin zone with a symmetry-enforced almost movable WNL, denoted in green, as predicted in Ref. [38]. The WNL interconnects adjacent N points (green dots). (b),(c) ARPES data and DFT calculation along the Γ-Σ direction. A band crossing corresponding to the WNL is highlighted with blue arrows. (d)–(f) ARPES data and DFT calculations along k_y taken at selected k_x near the location of the WNL. The energy distribution curves at $k_y = 0$ Å support a vanishing band splitting at the WNL, and q_0 denotes the position of the WNL along k_x. (g) ARPES constant-energy cuts recorded in the Γ-Σ plane ($h\nu = 618$ eV) at energies near the WNL (blue arrows).

the corresponding calculation in Fig. 1(c). For our analysis, we focus on the topmost valence band, which extends approximately 1.5 eV below E_F. This band exhibits a notable splitting resulting from spin-orbit coupling (SOC) and broken inversion symmetry, as confirmed by both our calculations and high-resolution data (see Supplemental Material [42] for further analysis). Interestingly, we observe a band crossing along the ΓΣ path, denoted by blue arrows in Figs. 1(b) and 1(c). Around the observed crossing at q_0, the band dispersion is highly anisotropic, and our data and calculations clearly reveal splittings along both in-plane momentum directions [Figs. 1(d)–1(g)].

Tracing q_0 along the out-of-plane momentum k_z, our DFT calculations reveal a Weyl-type—i.e., twofold spin-degenerate—nodal line (WNL) that connects neighboring N points through the ΓZNΣ mirror planes, as depicted in Figs. 1(a), 2(b), and 2(d). This finding confirms its classification as a so-called almost movable WNL, a new type of topological feature theoretically predicted to occur in certain nonsymmorphic crystals, among them, the space group $I4_1md$ (#109) [38]. Notably, almost movable WNL have a different physical origin than previously discussed movable nodal lines in nonsymmorphic systems [43] and than nodal lines pinned to high-symmetry directions [44]. As we will show later, almost movable WNL emerge as a source of unconventional orbital physics that is closely related to their topological properties.

To experimentally verify the k_z evolution, we conducted photon-energy-dependent measurements. We obtained data sets in two energy intervals, as illustrated in Fig. 2(b). Representative data sets in Fig. 2(a) are shown and compared to calculations at corresponding out-of-plane momenta [Fig. 2(c)], achieving excellent agreement. Notably, a gradual shift of the band crossing towards larger k_x is observed as k_z varies from the zone center ($h\nu = 618$ eV, $k_z \approx 0$) to the ZS equi-k_z plane ($h\nu = 668$ eV, $k_z \approx 2\pi/c$). Thus, our measurements and calculations reveal a significant undulation of the WNL with k_z, where the band crossing modulates between type II (tilted) and type I (untilted). Importantly, we consistently observe abrupt modulations in the photoemission intensity along k_x at the band crossing for all photon energies, providing an additional spectroscopic signature of the WNL. Taken together, we plot the WNL in Fig. 2(d) as extracted from the experimental data (see also Supplemental Material [42]), in good agreement with the overlaid calculations.

Having established the WNL dispersion, we next focus on the properties of the momentum-dependent orbital wave function in the vicinity of the WNL using CD and LD in ARPES. To this end, in Sec. II B, we recall the definitions of CD and LD, as well as the relation between both quantities. We further discuss specific aspects related to the experimental geometry and conditions.

B. General aspects of linear and circular dichroism in ARPES

We consider an experimental geometry with light incident in the xz plane under an incidence angle α;

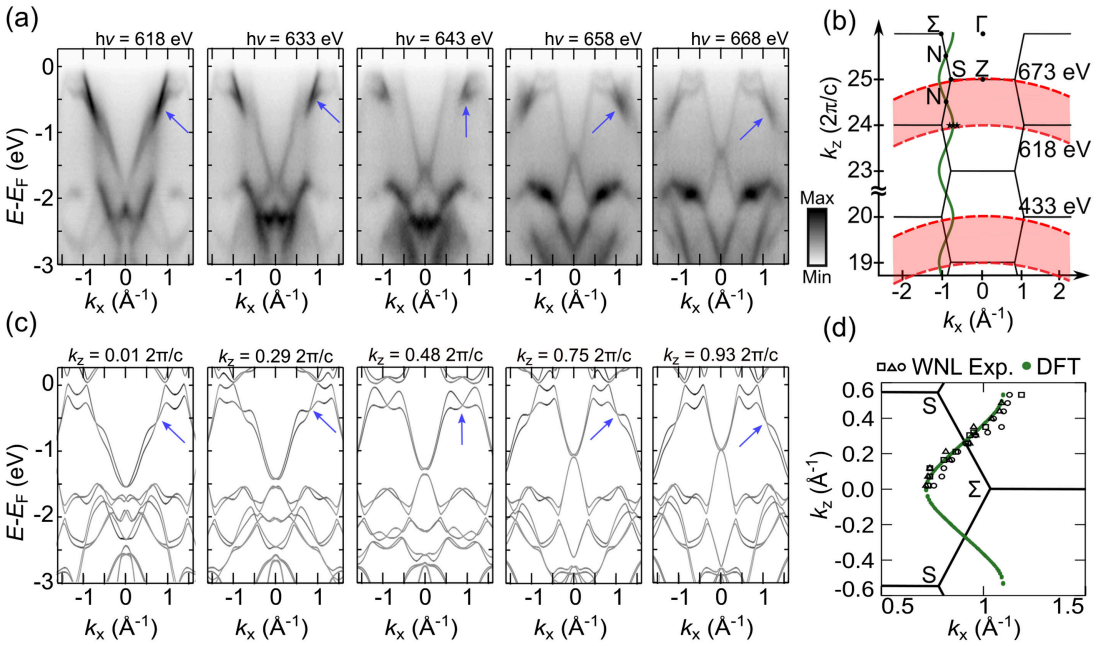

FIG. 2. Three-dimensional evolution of the Weyl nodal line. (a) ARPES data sets along the Γ-Σ direction for various k_z throughout the Brillouin zone. Data sets are symmetrized with respect to the Γ point. (b) Bulk Brillouin zone structure of TaAs. Red dashed lines represent measurements at fixed photon energy hν. Data sets were taken in the red-shaded area. The stars represent the cuts shown in Figs. 1(d)–1(f). (c) DFT calculations at k_z values matching the data sets in (a). Blue arrows mark the position of the WNL. (d) Position of the WNL based on DFT (green line) and hν-dependent ARPES data (data points) in the upper red-shaded area of panel (c).

see Fig. 3(d). The light electric field reads $\boldsymbol{\mathcal{E}}_{\mathbf{R,L}} = (\sin\alpha\mathcal{E}_x, \pm i\mathcal{E}_y, \cos\alpha\mathcal{E}_z)$. The CD is defined as the difference in intensity for two ARPES data sets I_R and I_L taken with right and left circularly polarized light:

$$\mathrm{CD}(k_x, k_y, E) = I_\mathrm{R}(k_x, k_y, E) - I_\mathrm{L}(k_x, k_y, E). \quad (1)$$

Similarly, we define the LD as the difference in intensity for two ARPES data sets I_+ and I_- taken with light incident along the positive and negative x directions, such that $\boldsymbol{\mathcal{E}}_\pm = (\pm\sin\alpha\mathcal{E}_x, E_y, \cos\alpha\mathcal{E}_z)$ and

$$\mathrm{LD}(k_x, k_y, E) = I_+(k_x, k_y, E) - I_-(k_x, k_y, E), \quad (2)$$

with $E_y = \pm i\mathcal{E}_y$ for circularly polarized light and $E_y = 0$ for p-polarized light. As we discuss in more detail below, this definition is sensible because it results in a close relation between the CD and LD signals. For the important case that the yz plane is a crystalline mirror plane, the LD may be written as

$$\mathrm{LD}(k_\mathrm{x}, k_\mathrm{y}, E) = I_+(k_x, k_y, E) - I_+(-k_x, k_y, E), \quad (3)$$

which describes the way the LD is usually measured, namely, as the $\pm k_x$ intensity asymmetry in a fixed experimental geometry [45,46].

We next recall expressions of the CD and LD in terms of the photoemission matrix elements $T_j = \langle\Psi_f|\mathcal{E}_j j|\Psi_i\rangle$, with $j = x, y, z$, and the photoemission initial and final states Ψ_i and Ψ_f. Then, the CD may be represented as

$$\mathrm{CD}(k_x, k_y) \propto \sin\alpha\mathfrak{I}(T_x^* T_y) + \cos\alpha\mathfrak{I}(T_y^* T_z). \quad (4)$$

We next focus on the xz and yz planes, assuming both are crystalline mirror planes, as is the case for TaAs(001). After appropriate consideration of symmetries in Eq. (4), for the CD in the yz plane, one obtains

$$\mathrm{CD}(0, k_y) \propto \cos\alpha\mathfrak{I}(T_y^* T_z). \quad (5)$$

For the LD in the xz plane, we find

$$\mathrm{LD}(k_x, 0) \propto \sin\alpha\cos\alpha\mathfrak{R}(T_x^* T_z). \quad (6)$$

In Eqs. (4)–(6), Im and Re refer to the imaginary and real parts, respectively. The close correspondence between Eqs. (5) and (6) shows that the LD along k_x and the CD along k_y contain similar information. Especially for C_4-symmetric systems, such as TaAs(001), they are proportional to the real and the imaginary part of the same product of matrix elements arising from the out-of-plane component $\mathcal{E}_z$ and the in-plane component $\mathcal{E}_{x,y}$ parallel to the in-plane wave vector $k_{x,y}$, which allows for a systematic comparison (cf. Fig. 3). From the expressions in Eqs. (5) and (6), it is apparent that the LD and CD can carry phase-sensitive information about the orbital wave functions Ψ_i and Ψ_f via the photoemission matrix elements. Indeed, it has been shown that dichroism in ARPES can provide sensitivity to the OAM of the photoemission initial state Ψ_i; see, e.g., Refs. [20,22,23,34,47–54].

We further exploit the mirror symmetries in TaAs(001) and consider the normalized CD (nCD), which we define as

$$\mathrm{nCD}(k_x, k_y) = \frac{1}{2}\frac{\mathrm{CD}(k_x, k_y) + \mathrm{CD}(-k_x, k_y)}{I_\mathrm{R}(k_x, k_y) + I_\mathrm{L}(k_x, k_y)}. \quad (7)$$

The nCD is normalized to the total intensity, and more importantly, the effect of oblique light incidence is removed, such that

$$\mathrm{nCD}(k_x, k_y) \propto \mathfrak{I}(T_y^* T_z). \quad (8)$$

The nCD thus recovers the CD signal expected for a perfectly grazing light incidence along x. This result is advantageous since the CD is sensitive to the OAM along the light propagation direction [49]; therefore, the nCD exclusively reflects the L_x OAM component. Hence, we consider the nCD in our analysis of the OAM texture in the full (k_x, k_y) plane in Figs. 4(d)–4(e).

We conclude this section by discussing some experimental considerations specific to the setup and experimental geometry used in this study. The angular dispersive direction of the spectrometer is along x, so $\mathrm{LD}(k_x, 0)$ is measured in parallel without the need for scanning lens parameters. This process enables a more efficient data acquisition for $\mathrm{LD}(k_x, 0)$ than for $\mathrm{CD}(0, k_y)$, which requires deflector-lens scans (see the Appendix for a description of the experimental details). Therefore, high-resolution data sets are obtained for $\mathrm{LD}(k_x, 0)$ (cf. Fig. 3). In our experiments, only circularly polarized soft x rays are available. The LD is more commonly considered for p-polarized light. However, in the xz mirror plane, the LD measured with circularly polarized light is the same as the one for p-polarized light because the CD necessarily vanishes in the xz mirror plane, implying that the matrix elements of $\mathcal{E}_x$ and $\mathcal{E}_z$ add up incoherently with those of $\mathcal{E}_y$. Therefore, the $\mathcal{E}_y$ component, for symmetry reasons, does not influence the LD in the xz mirror plane [46]. We restrict the analysis of the LD to the plane of light incidence whereas the CD is considered in the complete $k_x k_y$ plane (see Fig. 4).

C. Dichroism and OAM reversal at Weyl nodal line

We now explore the orbital texture of the WNL and examine the calculated orbital character of the Bloch states Ψ_k on the $\Gamma\Sigma$ line. Along k_x, we find dominant contributions from Ta d_{xz} and $d_{z^2}/d_{x^2-y^2}$ orbitals. Because of the broken inversion symmetry, these orbitals hybridize with complex phases:

$$|\Psi_k\rangle \propto (\sqrt{3}|d_{z^2}\rangle + |d_{x^2-y^2}\rangle) + i\gamma(\mathbf{k}) \cdot |d_{xz}\rangle.$$

As a result, the states Ψ_k carry a finite atomic OAM, $\langle L_y \rangle \propto \gamma(k)$. Interestingly, $\gamma(k)$ and the OAM $\langle L_y \rangle$ reverse sign as k_x varies across the WNL [Fig. 3(a)], indicating a highly momentum-dependent OAM texture in the vicinity of the WNL.

To address this finding experimentally, we next consider the LD in ARPES along k_x on the ΓΣ line ($h\nu = 618$ eV) [Fig. 3(b)]. Strikingly, the measured LD closely follows the behavior of the calculated OAM and shows a pronounced sign reversal across the WNL. We find that the effect persists upon variation of the photon energy [Figs. 4(b) and S4], demonstrating that the photoelectron final state Ψ_f plays only a minor role. We attribute the observed sign reversal of the LD to the sign change in $\gamma(k)$ as a result of the term

$$\mathrm{LD}(k_x) \propto \Re(\langle \Psi_f | \mathcal{E}_x x | d_{xz} \rangle^* \langle \Psi_f | \mathcal{E}_z z | \sqrt{3} d_{z^2} + d_{x^2-y^2} \rangle). \quad (9)$$

From Eq. (9), one finds $\mathrm{LD}(k_x, 0) \propto \gamma(k_x) \propto \langle L_y \rangle$. While the general expression for the LD in Eq. (6) contains additional contributions, the close match between measured LD and calculated OAM indicates that the term in Eq. (9) is dominant in our experiments.

To further support this finding, we perform one-step photoemission calculations [Fig. 3(c)]. The results show an excellent agreement with the experimental data, confirming that the observed LD reversal at the WNL is indeed a genuine effect of the photoemission matrix element. A minor exception is the appearance of a surface resonance in the calculation that is not observed in the experimental data. A comparison of LD distributions along ΓΣ at different photon energies confirms a modest influence of the photoemission final state (see Fig. S4 in Ref. [42]). Both the calculations and experimental data consistently demonstrate a reversal of the LD at the WNL, highlighting the sensitivity of the LD to the phase $\gamma(k)$ and to the OAM, with only minor contributions from geometric or final-state effects. Figure 3(f) presents a quantitative comparison between the measured and calculated intensities, showing momentum distribution curves at energies above and below the WNL. We observe pronounced left-right intensity asymmetries of up to 35%, which lead to the LD seen in Fig. 3(b). As before, we find strong agreement between experiment and theory, both in terms of relative intensity variations and spectral line shapes.

Based on the close correspondence between $\mathrm{LD}(k_x, 0)$ and CD, discussed in the previous section, we expect that the CD also reflects the momentum dependence of the phase γ. Indeed, our measurements in Fig. 3(e) confirm this expectation and show that the CD switches sign close to the WNL, although the CD data do not reach the excellent quality of the LD data in our experimental geometry (cf. Sec. II B). Taken together, our systematic LD and CD data, supported by calculations, demonstrate a sign reversal of the OAM across the WNL.

D. Orbital vortex lines in 3D momentum space

To understand the observed OAM behavior, we explore the detailed OAM texture in the vicinity of the WNL. For this purpose, we consider the Hamiltonian

$$\mathcal{H}_{\mathrm{OVL}}(\mathbf{q}) = \mathcal{H}_0 + H_{\mathrm{ISB}}(\mathbf{q}), \quad (10)$$

where $\mathbf{q} = \mathbf{k} - \mathbf{q}_0$ and the WNL is located at $\mathbf{q}_0$ (see Supplemental Material [42]). Note that $\mathcal{H}_0$ describes the unperturbed situation, and the second term accounts for the formation of OAM $\mathbf{L}$ due to broken inversion symmetry. At first order, the latter can be expressed as

$$\mathcal{H}_{\mathrm{ISB}}(\mathbf{q}) \approx -\alpha_{y,x} q_y L_x + (\alpha_{x,y} q_x - \alpha_{z,y} q_z) L_y + \alpha_{y,z} q_y L_z. \quad (11)$$

The coefficients $\alpha_{i,j}$ are real-valued parameters, and they quantify the energy scale associated with the breaking of inversion symmetry.

Mirror symmetry M_y forces the OAM components L_x and L_z to flip sign at $q_y = 0$, i.e., at the $k_x k_z$ mirror plane. The observed sign change of L_y within this plane (Fig. 3) results from a combination of mirror- and time-reversal symmetry. This case is illustrated schematically in Fig. 4(a): Moving from an arbitrary momentum $\mathbf{k}'$ relative to the time-reversal invariant N point to its Kramer's partner $-\mathbf{k}'$, the OAM L_y must change sign at one k point on any path in the mirror plane. The collection of these points forms a line where the OAM vanishes.

In Fig. 4(b), we present the calculated OAM $\langle L_y \rangle$ component in the $k_x k_z$ mirror plane. In agreement with our model calculation, the OAM flips sign on a curved trajectory $\mathbf{q_0}(k_z)$ (where $L = 0$) that perfectly aligns with the WNL (green line). To explore this result experimentally, we consider LD data collected with varied photon energy [Fig. 4(c)]. Consistent with the calculated OAM in Fig. 4(b) and with the observed evolution of the WNL in Fig. 2, we find that the sign reversal of the LD progressively shifts towards larger k_x as k_z varies from the ΓΣ to the ZS high-symmetry line. This observation establishes the k_z-dependent undulation of the OAM texture within the ΓΣZ mirror plane.

Taking all terms in Eq. (11) into account, the resulting OAM texture exhibits a vortex enclosing the line $\mathbf{q_0}(k_z)$. Although details depend on the k_z-dependent parameters $\alpha_{i,j}$, the OAM vortex universally carries a winding number $\nu = 1$. Our DFT calculations confirm these findings [see Figs. 4(a) and S6] and further show that $\alpha_{y,z}$ is small for all k_z, implying that $\mathbf{L}$ has predominantly in-plane orientation.

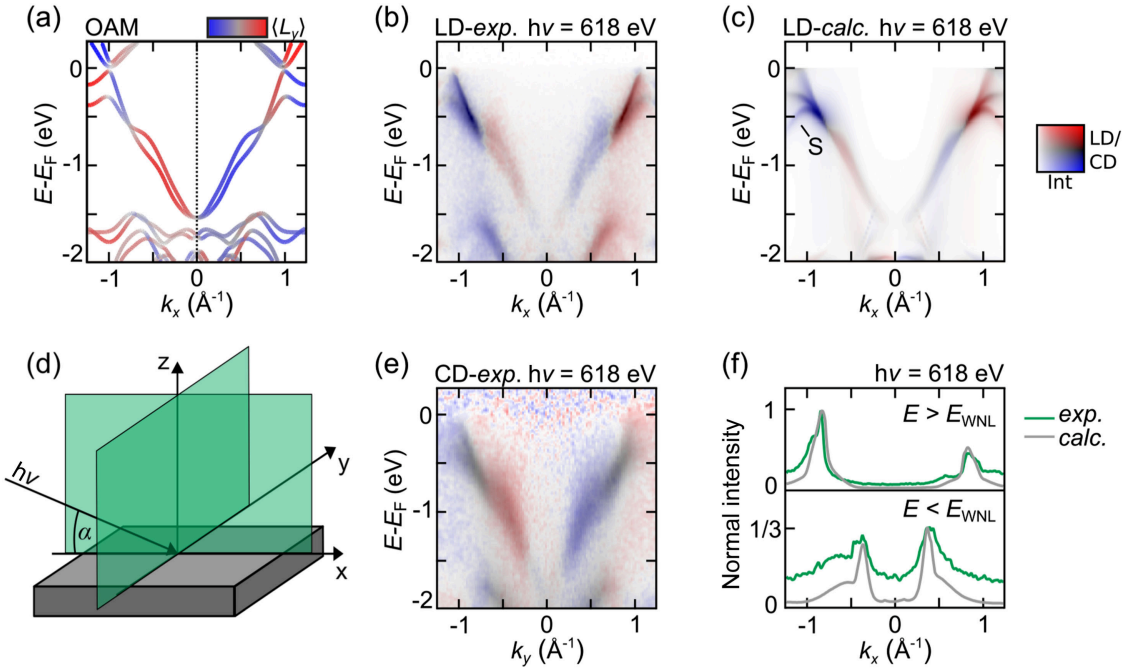

FIG. 3. Linear dichroism and orbital angular momentum at the WNL. (a) OAM L_y, as obtained from DFT. (b) Measured linear dichroism (see text) at $h\nu = 618$ eV corresponding to an out-of-plane momentum of $k_z \approx 0$. (c) Same as in panel (b) but obtained from a one-step photoemission calculation. Overall, the LD shows a sign change at the WNL crossing point, in agreement with OAM (see Fig. S4 of Ref. [42] for LD data at a different photon energy corresponding to the equivalent k_z). A surface resonance—obtained only in the LD calculation in panel (c)—is marked by *S*. (d) Experimental geometry. (e) Circular dichroism (see text) at $h\nu = 618$ eV along k_y. (f) Photoemission intensity momentum distribution curves at energies $E - E_F = -0.4$ eV and $E - E_F = -1.1$ eV, which are above and below the WNL crossing point, respectively.

Notably, given Eqs. (10) and (11), there is one final ingredient missing in order to obtain the fully fledged WNL, which is spin-orbit coupling. This factor lifts spin degeneracy implicit in the band structure obtained from Eq. (11). The nontrivial OAM winding texture, however, remains unaffected by the presence of SOC (see also Supplemental Material [42]). In essence, the line $\mathbf{q_0}(k_z)$ serves as a precursor of the WNL, around which $H_{SOC} \propto \mathbf{L} \cdot \mathbf{S}$ induces a band splitting $\Delta E \propto L$ that vanishes at $\mathbf{q_0}$.

To gain experimental access to the OAM vortex, we now consider $k_x k_y$ momentum distributions of the nCD, as introduced in Eq. (7) in Sec. II B. The nCD for light incident in the xz plane is sensitive to the L_x component of the OAM. Given the predicted OAM texture in Fig. 4(a), it is also important to address the L_y component, which can be achieved by changing the plane of light incidence from the xz to the yz plane. We refer to nCD data sets corresponding to light incidence in the xz and yz planes as $\mathrm{nCD}_{0°}$ and $\mathrm{nCD}_{90°}$, respectively. In general, acquiring these two data sets requires adjusting the experimental geometry. However, for TaAs(001), we take advantage of the fourfold rotational symmetry, which ensures that $\mathrm{nCD}_{90°}(k_x, k_y) = \mathrm{nCD}_{0°}(-k_y, k_x)$. As a result, we obtain $\mathrm{nCD}_{90°}$ immediately from the $\mathrm{nCD}_{0°}$ data, enabling us to analyze the dichroic vector field $(\mathrm{nCD}_{0°}, \mathrm{nCD}_{90°})$. The latter serves as a probe of the in-plane OAM texture (L_x, L_y), which follows the same symmetry relation as the nCD, $L_y(k_x, k_y) = L_x(-k_y, k_x)$.

The momentum distributions resulting from this analysis are shown in Figs. 4(d) and 4(e). We examine data sets collected at two different photon energies, corresponding to distinct k_z values, and at the binding energy of the WNL for each respective k_z. The red-blue color denotes the $\mathrm{nCD}_{0°}$ signal, and the arrows represent the dichroic vector field $(\mathrm{nCD}_{0°}, \mathrm{nCD}_{90°})$. In both data sets, (d) and (e), the characteristic sign reversal of the dichroism along the k_y axis is visible, consistent with Fig. 3(e). More importantly, vortex textures in the dichroic vector field are observed near the four WNL positions, highlighted by green circles. These textures indicate a finite circulation of the dichroic vector field along loops surrounding the WNL, providing direct evidence of vorticity in the wave-function phase around the WNL. These results are in agreement with the expected OAM texture (L_x, L_y), as predicted from our model Hamiltonian in Eq. (11) and DFT calculations [Fig. 4(a)]. A comparison between the measured dichroic vector field and the calculated OAM texture in proximity of the WNL is shown in Fig. S6 of the Supplementary Material. The vortex texture is observed for both exemplary k_z momenta considered here, with the positions of the vortex cores $\mathbf{q_0}$ varying according to the undulation of the

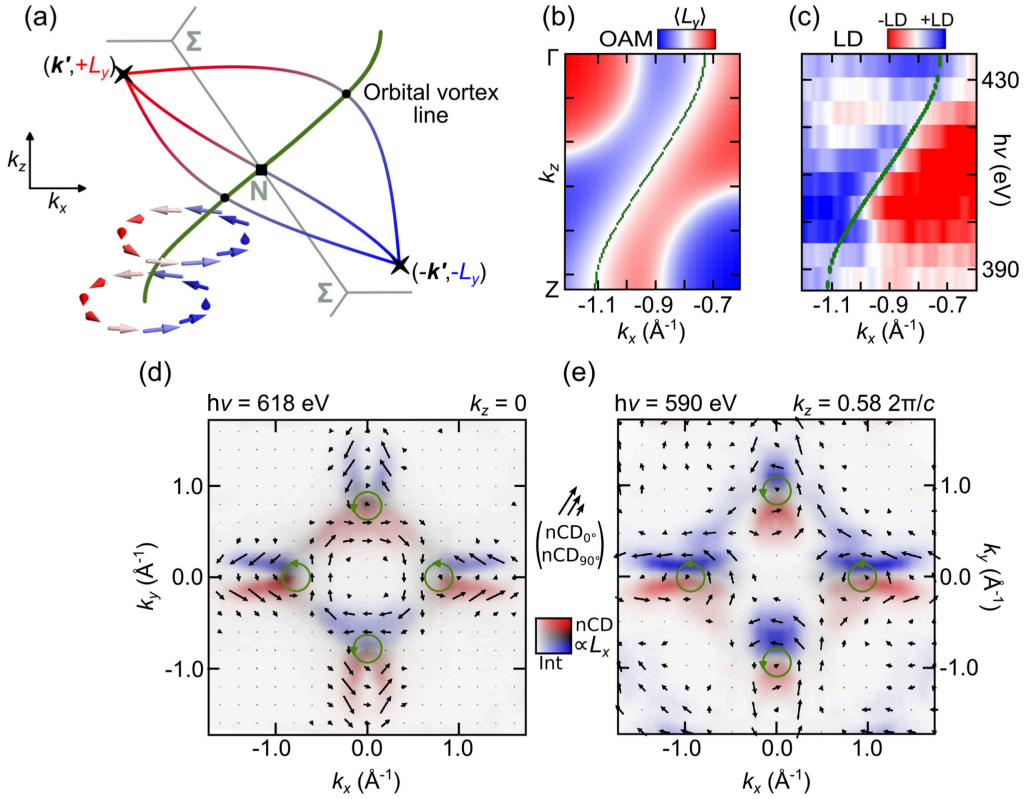

FIG. 4. Orbital vortex line in three-dimensional momentum space. (a) Illustration of symmetry-enforced formation of orbital vortex lines. DFT calculations of the OAM vortex configuration are depicted at different k_z values. (b) DFT calculation of the OAM in the ΓZNΣ mirror plane. The green line indicates the calculated position of the WNL, matching the trajectory on which the OAM vanishes. (c) Measured LD, integrated over the energy interval of the orbital vortex line, in dependence of photon energy $h\nu$, sampling the sign change of the LD for different k_z values throughout one BZ. (d),(e) Normalized circular dichroism momentum distributions obtained at photon energies $h\nu = 618$ eV and $h\nu = 590$ eV, corresponding to out-of-plane momenta of $k_z \approx 0$ and $k_z \approx 0.582\pi/c$, respectively. The constant energy contours are taken at the respective energy of the WNL, i.e., −0.58 eV (d) and −0.38 eV (e). The red and blue colors denote the nCD_{0° signal, and the arrows represent the dichroic vector field $(\mathrm{nCD}_{0^\circ}, \mathrm{nCD}_{90^\circ})$ (see text for details). The dichroic vector field forms vortex textures around the four WNL positions, highlighted by the green circles.

WNL [Figs. 2(d), 4(b), and 4(c)]. Taken collectively, our experimental data in Figs. 3 and 4 visualize OAM winding at the WNL across full 3D momentum space.

III. CONCLUSIONS

In conclusion, our work provides a three-dimensional imaging of orbital vortex lines in the electronic structure of a topological quantum material. These lines in momentum space exhibit a nontrivial winding in the phase of the orbital wave function, which is accompanied by a vortexlike texture of the OAM. The measured orbital-phase winding in the three-dimensional Bloch wave-function manifold directly visualizes the topological charge of a Weyl nodal line and is thus closely tied to band topology.

Our results establish bimodal dichroism in bulk-sensitive SX-ARPES as a robust approach to map the complete orbital texture in 3D materials [52]. We demonstrate its potential as a powerful tool for probing topological physics in quantum materials by directly visualizing the topological phase winding at nodal lines. Furthermore, our findings reveal, for the first time experimentally, almost movable Weyl nodal lines, representing a novel form of symmetry-enforced band degeneracy [38]. The application of dichroic photoemission in 3D momentum space could open new pathways for investigating exotic band topologies driven by line nodes, including nodal chains, nexus textures, and non-Abelian topological invariants [5,43,55], which have remained elusive in the study of realistic materials so far.

Finally, we emphasize that our discovery of orbital vortices raises the prospect of exploring novel quantum transport phenomena. Specifically, our results highlight the potential of investigating 3D quantum materials in the context of orbitronics [39–41]. Orbital textures—as observed in our work—in turn underlie orbitronic phenomena at the microscopic level, including the orbital Hall effect and the orbital Edelstein effect. This feature underscores the broad relevance of achieving comprehensive

momentum-resolved access to OAM, for which this study sets a new benchmark.

ACKNOWLEDGMENTS

D. D. S., G. S., and L. C. thank Chiara Pacella for useful discussions. This work is funded by the Deutsche Forschungsgemeinschaft (DFG, German Research Foundation) through SFB 1170 ToCoTronics, the Würzburg-Dresden Cluster of Excellence on Complexity and Topology in Quantum Matter–*ct.qmat* Project-ID 390858490—EXC 2147, and RE1469/13-2. H. B. acknowledges support from the Research Council of Norway (RCN) through its Centres of Excellence funding scheme, Project No. 262633, "QuSpin," and RCN Project No. 323766. The research leading to these results has received funding from the European Union's Horizon 2020 research and innovation program under the Marie Skłodowska-Curie Grant Agreement No. 897276. We acknowledge DESY (Hamburg, Germany), a member of the Helmholtz Association HGF, for the provision of experimental facilities. Parts of this research were carried out at PETRA III, and we would like to thank Kai Bagschik, Jens Viefhaus, Frank Scholz, Jörn Seltmann, and Florian Trinter for assistance in using Beamline P04. Funding for the photoemission spectroscopy instrument at Beamline P04 (Contract No. 05KS7FK2, No. 05K10FK1, No. 05K12FK1, No. 05K13FK1, and No. 05K19FK4 with Kiel University; No. 05KS7WW1, No. 05K10WW2, and No. 05K19WW2 with Würzburg University) by the Federal Ministry of Education and Research (BMBF) is gratefully acknowledged. J. S. would like to acknowledge Ján Minár for providing a computational cluster at NTC, University of West Bohemia. We gratefully acknowledge the Gauss Centre for Supercomputing e.V. for funding this project by providing computing time on the GCS Supercomputer SuperMUC at Leibniz Supercomputing Centre. J. N. and T. S. acknowledge support from the National Research Foundation, under Grant No. NSF DMR-1606952. The crystal synthesis and characterization was carried out at the National High Magnetic Field Laboratory, which is funded by the National Science Foundation (NSF DMR-2128556) and the State of Florida.

T. F. and M. Ü. performed the experiments, with support from H. B., B. G., P. K., J. B., M. H., M. K., and K. R. T. F. and M. Ü. analyzed the experimental data supported by P. K. P. E. performed the first-principles calculations. J. S. performed the one-step photoemission calculations. J. N. N., T. F., and T. S. synthesized and characterized the TaAs samples. M. Ü. and L. K. L. developed the model Hamiltonian with support from T. F. and P. K. All authors contributed to the interpretation and discussion of the results. T. F., M. Ü., and H. B. wrote the manuscript with contributions from P. E., L. C., J. S., G. S., D. dS., L. K. L., R. M., and F. R. M. Ü. and H. B. conceived and planned the project.

APPENDIX: EXPERIMENTAL AND THEORETICAL DETAILS

SX-ARPES experiments were carried out at the ASPHERE III endstation at the Variable Polarization XUV Beamline P04 of the PETRA III storage ring at DESY (Hamburg, Germany). ARPES data were collected at sample temperatures of approximately 50 K, and the energy resolution of the ARPES measurements was set to $\Delta E \approx 60$ meV for higher resolution measurements [Figs. 1(b), 2(a), and 3] and $\Delta E \approx 90$ meV for momentum maps [Figs. 1(d)–1(g) and 4]. We used the deflection mode of the SCIENTA DA30-L analyzer, allowing for data acquisition in a fixed sample geometry. Light incidence was within the xz analyzer slit plane at an angle of $\alpha \approx 20°$ to the sample surface [see Fig. 3(d)]. TaAs single crystals were cleaved *in situ* with a top post at a temperature below 100 K and a pressure better than 5×10^{-9} mbar. Details on chemical vapor transport growth of TaAs single crystals can be found in Ref. [20].

In our theoretical study, we considered the noncentrosymmetric primitive unit cell of TaAs (space group $I4_1md$) with a lattice constant of 6.355 Å. We employed state-of-the-art first-principles calculations based on density functional theory as implemented in the Vienna *Ab initio* Simulation Package [56], within the projector-augmented-plane-wave method [57,58]. The generalized gradient approximation as parametrized by the PBE-GGA functional for the exchange-correlation potential was used [59] by expanding the Kohn-Sham wave functions into plane waves up to an energy cutoff of 400 eV. We sampled the Brillouin zone on an $8 \times 8 \times 8$ regular mesh by including SOC self-consistently [60]. For the calculation of the OAM, the Kohn-Sham wave functions were projected onto a Ta s, p, d- and As s, p-type tesseral harmonics basis as implemented in the WANNIER90 suite [61]. The OAM expectation values were then obtained in the atomic centered approximation by rotating the tesseral harmonics basis into the eigenbasis of the OAM operator, i.e., the spherical harmonics.

The one-step model photoemission calculations were performed within the spin-polarized-relativistic Korringa-Kohn-Rostoker package based on Green's function formalism. We used the same structural input and exchange-correlation potential as in Ref. [53]. The calculations gave us access to a photoemission signal with an accurate angular dependence of ARPES spectral weight by taking into account experimental geometry, energy, and polarization of photons as well as a multiply-scattered final state with a given surface termination.

[1] K. S. Novoselov, A. K. Geim, S. V. Morozov, D. Jiang, M. I. Katsnelson, I. V. Grigorieva, S. V. Dubonos, and A. A. Firsov, *Two-dimensional gas of massless Dirac fermions in graphene*, Nature (London) **438**, 197 (2005).

[2] M. Z. Hasan and C. L. Kane, *Colloquium: Topological insulators*, Rev. Mod. Phys. **82**, 3045 (2010).
[3] X.-L. Qi and S.-C. Zhang, *Topological insulators and superconductors*, Rev. Mod. Phys. **83**, 1057 (2011).
[4] A. A. Burkov, M. D. Hook, and L. Balents, *Topological nodal semimetals*, Phys. Rev. B **84**, 235126 (2011).
[5] T. T. Heikkilä and G. E. Volovik, *Nexus and Dirac lines in topological materials*, New J. Phys. **17**, 093019 (2015).
[6] C. Fang, Y. Chen, H.-Y. Kee, and L. Fu, *Topological nodal line semimetals with and without spin-orbital coupling*, Phys. Rev. B **92**, 081201(R) (2015).
[7] C.-K. Chiu, J. C. Y. Teo, A. P. Schnyder, and S. Ryu, *Classification of topological quantum matter with symmetries*, Rev. Mod. Phys. **88**, 035005 (2016).
[8] B. Bradlyn, J. Cano, Z. Wang, M. G. Vergniory, C. Felser, R. J. Cava, and B. A. Bernevig, *Beyond Dirac and Weyl fermions: Unconventional quasiparticles in conventional crystals*, Science **353**, aaf5037 (2016).
[9] C. Fang, H. Weng, X. Dai, and Z. Fang, *Topological nodal line semimetals*, Chin. Phys. B **25**, 117106 (2016).
[10] F. D. M. Haldane, *Nobel Lecture: Topological quantum matter*, Rev. Mod. Phys. **89**, 040502 (2017).
[11] X.-G. Wen, *Colloquium: Zoo of quantum-topological phases of matter*, Rev. Mod. Phys. **89**, 041004 (2017).
[12] N. P. Armitage, E. J. Mele, and A. Vishwanath, *Weyl and Dirac semimetals in three-dimensional solids*, Rev. Mod. Phys. **90**, 015001 (2018).
[13] T. Ozawa, H. M. Price, A. Amo, N. Goldman, M. Hafezi, L. Lu, M. C. Rechtsman, D. Schuster, J. Simon, O. Zilberberg, and I. Carusotto, *Topological photonics*, Rev. Mod. Phys. **91**, 015006 (2019).
[14] J.-W. Rhim, K. Kim, and B.-J. Yang, *Quantum distance and anomalous Landau levels of flat bands*, Nature (London) **584**, 59 (2020).
[15] M. A. Wilde, M. Dodenhöft, A. Niedermayr, A. Bauer, M. M. Hirschmann, K. Alpin, A. P. Schnyder, and C. Pfleiderer, *Symmetry-enforced topological nodal planes at the Fermi surface of a chiral magnet*, Nature (London) 2021) 374 ,**594**).
[16] D. Hsieh, Y. Xia, L. Wray, D. Qian, A. Pal, J. H. Dil, J. Osterwalder, F. Meier, G. Bihlmayer, C. L. Kane, Y. S. Hor, R. J. Cava, and M. Z. Hasan, *Observation of unconventional quantum spin textures in topological insulators*, Science **323**, 919 (2009).
[17] Y. Liu, G. Bian, T. Miller, and T.-C. Chiang, *Visualizing electronic chirality and Berry phases in graphene systems using photoemission with circularly polarized light*, Phys. Rev. Lett. **107**, 166803 (2011).
[18] B. Q. Lv, H. M. Weng, B. B. Fu, X. P. Wang, H. Miao, J. Ma, P. Richard, X. C. Huang, L. X. Zhao, G. F. Chen, Z. Fang, X. Dai, T. Qian, and H. Ding, *Experimental discovery of Weyl semimetal* TaAs, Phys. Rev. X **5**, 031013 (2015).
[19] S.-Y. Xu, I. Belopolski, N. Alidoust, M. Neupane, G. Bian, C. Zhang, R. Sankar, G. Chang, Z. Yuan, C.-C. Lee, S.-M. Huang, H. Zheng, J. Ma, D. S. Sanchez, B. Wang, A. Bansil, F. Chou, P. P. Shibayev, H. Lin, S. Jia, and M. Z. Hasan, *Discovery of a Weyl fermion semimetal and topological Fermi arcs*, Science **349**, 613 (2015).
[20] M. Ünzelmann, H. Bentmann, T. Figgemeier, P. Eck, J. N. Neu, B. Geldiyev, F. Diekmann, S. Rohlf, J. Buck, M. Hoesch, M. Kalläne, K. Rossnagel, R. Thomale, T. Siegrist, G. Sangiovanni, D. D. Sante, and F. Reinert, *Momentum-space signatures of Berry flux monopoles in the Weyl semimetal* TaAs, Nat. Commun. **12**, 3650 (2021).
[21] N. B. Schröter, S. Stolz, K. Manna, F. De Juan, M. G. Vergniory, J. A. Krieger, D. Pei, T. Schmitt, P. Dudin, T. K. Kim *et al.*, *Observation and control of maximal Chern numbers in a chiral topological semimetal*, Science **369**, 179 (2020).
[22] Y. Yen, J. A. Krieger, M. Yao, I. Robredo, K. Manna, Q. Yang, E. C. McFarlane, C. Shekhar, H. Borrmann, S. Stolz, R. Widmer, O. Gröning, V. N. Strocov, S. S. P. Parkin, C. Felser, M. G. Vergniory, M. Schüler, and N. B. M. Schröter, *Controllable orbital angular momentum monopoles in chiral topological semimetals*, Nat. Phys. **20**, 1912 (2024).
[23] S. S. Brinkman, X. L. Tan, B. Brekke, A. C. Mathisen, O. Finnseth, R. J. Schenk, K. Hagiwara, M.-J. Huang, J. Buck, M. Kalläne, M. Hoesch, K. Rossnagel, K.-H. Ou Yang, M.-T. Lin, G.-J. Shu, Y.-J. Chen, C. Tusche, and H. Bentmann, *Chirality-driven orbital angular momentum and circular dichroism in* CoSi, Phys. Rev. Lett. **132**, 196402 (2024).
[24] J. A. Krieger, S. Stolz, I. Robredo, K. Manna, E. C. McFarlane, M. Date, B. Pal, J. Yang, E. B. Guedes, J. H. Dil *et al.*, *Weyl spin-momentum locking in a chiral topological semimetal*, Nat. Commun. **15**, 3720 (2024).
[25] G. E. Volovik, *The Universe in a Helium Droplet*, Vol. 117 (Oxford University Press, Oxford, 2003).
[26] A. A. Abrikosov, *The magnetic properties of superconducting alloys*, J. Phys. Chem. Solids **2**, 199 (1957).
[27] T. W. B. Kibble, *Topology of cosmic domains and strings*, J. Phys. A **9**, 1387 (1976).
[28] A. Vilenkin and E. P. S. Shellard, *Cosmic Strings and Other Topological Defects* (Cambridge University Press, Cambridge, England, 1994).
[29] L.-K. Lim and R. Moessner, *Pseudospin vortex ring with a nodal line in three dimensions*, Phys. Rev. Lett. **118**, 016401 (2017).
[30] K. Kim, J. Seo, E. Lee, K.-T. Ko, B. S. Kim, B. G. Jang, J. M. Ok, J. Lee, Y. J. Jo, W. Kang, J. H. Shim, C. Kim, H. W. Yeom, B. I. Min, B.-J. Yang, and J. S. Kim, *Large anomalous Hall current induced by topological nodal lines in a ferromagnetic van der Waals semimetal*, Nat. Mater. **17**, 794 (2018).
[31] H. T. Hirose, T. Terashima, T. Wada, Y. Matsushita, Y. Okamoto, K. Takenaka, and S. Uji, *Real spin and pseudospin topologies in the noncentrosymmetric topological nodal-line semimetal* CaAgAs, Phys. Rev. B **101**, 245104 (2020).
[32] H. Kim, J. M. Ok, S. Cha, B. G. Jang, C. I. Kwon, Y. Kohama, K. Kindo, W. J. Cho, E. S. Choi, Y. J. Jo, W. Kang, J. H. Shim, K. S. Kim, and J. S. Kim, *Quantum transport evidence of isolated topological nodal-line fermions*, Nat. Commun. **13**, 7188 (2022).
[33] S. W. Jung, S. H. Ryu, W. J. Shin, Y. Sohn, M. Huh, R. J. Koch, C. Jozwiak, E. Rotenberg, A. Bostwick, and K. S. Kim, *Black phosphorus as a bipolar pseudospin semiconductor*, Nat. Mater. **19**, 277 (2020).
[34] S. Beaulieu, J. Schusser, S. Dong, M. Schüler, T. Pincelli, M. Dendzik, J. Maklar, A. Neef, H. Ebert, K. Hricovini,

M. Wolf, J. Braun, L. Rettig, J. Minár, and R. Ernstorfer, *Revealing hidden orbital pseudospin texture with time-reversal dichroism in photoelectron angular distributions*, Phys. Rev. Lett. **125**, 216404 (2020).

[35] S.-M. Huang, S.-Y. Xu, I. Belopolski, C.-C. Lee, G. Chang, B. Wang, N. Alidoust, G. Bian, M. Neupane, C. Zhang, S. Jia, A. Bansil, H. Lin, and M. Z. Hasan, *A Weyl Fermion semimetal with surface Fermi arcs in the transition metal monopnictide* TaAs *class*, Nat. Commun. **6**, 7373 (2015).

[36] H. Weng, C. Fang, Z. Fang, B. A. Bernevig, and X. Dai, *Weyl semimetal phase in noncentrosymmetric transition-metal monophosphides*, Phys. Rev. X **5**, 011029 (2015).

[37] L. X. Yang, Z. K. Liu, Y. Sun, H. Peng, H. F. Yang, T. Zhang, B. Zhou, Y. Zhang, Y. F. Guo, M. Rahn, D. Prabhakaran, Z. Hussain, S.-K. Mo, C. Felser, B. Yan, and Y. L. Chen, *Weyl semimetal phase in the non-centrosymmetric compound* TaAs, Nat. Phys. **11**, 728 (2015).

[38] M. M. Hirschmann, A. Leonhardt, B. Kilic, D. H. Fabini, and A. P. Schnyder, *Symmetry-enforced band crossings in tetragonal materials: Dirac and Weyl degeneracies on points, lines, and planes*, Phys. Rev. Mater. **5**, 054202 (2021).

[39] B. A. Bernevig, T. L. Hughes, and S.-C. Zhang, *Orbitronics: The intrinsic orbital current in p-doped silicon*, Phys. Rev. Lett. **95**, 066601 (2005).

[40] D. Go, D. Jo, H.-W. Lee, M. Kläui, and Y. Mokrousov, *Orbitronics: Orbital currents in solids*, Europhys. Lett. **135**, 37001 (2021).

[41] Y.-G. Choi, D. Jo, K.-H. Ko, D. Go, K.-H. Kim, H. G. Park, C. Kim, B.-C. Min, G.-M. Choi, and H.-W. Lee, *Observation of the orbital Hall effect in a light metal* Ti, Nature (London) **619**, 52 (2023).

[42] See Supplemental Material at http://link.aps.org/supplemental/10.1103/PhysRevX.15.011032 for [brief description].

[43] T. Bzdušek, Q. Wu, A. Rüegg, M. Sigrist, and A. A. Soluyanov, *Nodal-chain metals*, Nature (London) **538**, 75 (2016).

[44] L. Wu, F. Tang, and X. Wan, *Exhaustive list of topological hourglass band crossings in 230 space groups*, Phys. Rev. B **102**, 035106 (2020).

[45] J. Henk, M. Hoesch, J. Osterwalder, A. Ernst, and P. Bruno, *Spin-orbit coupling in the L-gap surface states of* Au(111)*: Spin-resolved photoemission experiments and first-principles calculations*, J. Phys. Condens. Matter **16**, 7581 (2004).

[46] H. Bentmann, H. Maaß, E. E. Krasovskii, T. R. F. Peixoto, C. Seibel, M. Leandersson, T. Balasubramanian, and F. Reinert, *Strong linear dichroism in spin-polarized photoemission from spin-orbit-coupled surface states*, Phys. Rev. Lett. **119**, 106401 (2017).

[47] S. R. Park, C. H. Kim, J. Yu, J. H. Han, and C. Kim, *Orbital-angular-momentum based origin of Rashba-type surface band splitting*, Phys. Rev. Lett. **107**, 156803 (2011).

[48] S. R. Park, J. Han, C. Kim, Y. Y. Koh, C. Kim, H. Lee, H. J. Choi, J. H. Han, K. D. Lee, N. J. Hur, M. Arita, K. Shimada, H. Namatame, and M. Taniguchi, *Chiral orbital-angular momentum in the surface states of* Bi_2Se_3, Phys. Rev. Lett. **108**, 046805 (2012).

[49] J.-H. Park, C. H. Kim, J.-W. Rhim, and J. H. Han, *Orbital Rashba effect and its detection by circular dichroism angle-resolved photoemission spectroscopy*, Phys. Rev. B **85**, 195401 (2012).

[50] M. Schüler, U. D. Giovannini, H. Hübener, A. Rubio, M. A. Sentef, and P. Werner, *Local Berry curvature signatures in dichroic angle-resolved photoelectron spectroscopy from two-dimensional materials*, Sci. Adv. **6**, eaay2730 (2020).

[51] M. Ünzelmann, H. Bentmann, P. Eck, T. Kißlinger, B. Geldiyev, J. Rieger, S. Moser, R. C. Vidal, K. Kißner, L. Hammer, M. A. Schneider, T. Fauster, G. Sangiovanni, D. Di Sante, and F. Reinert, *Orbital-driven Rashba effect in a binary honeycomb monolayer* AgTe, Phys. Rev. Lett. **124**, 176401 (2020).

[52] M. Schüler, T. Pincelli, S. Dong, T. P. Devereaux, M. Wolf, L. Rettig, R. Ernstorfer, and S. Beaulieu, *Polarization-modulated angle-resolved photoemission spectroscopy: Toward circular dichroism without circular photons and Bloch wave-function reconstruction*, Phys. Rev. X **12**, 011019 (2022).

[53] J. Schusser, H. Bentmann, M. Ünzelmann, T. Figgemeier, C.-H. Min, S. Moser, J. N. Neu, T. Siegrist, and F. Reinert, *Assessing nontrivial topology in Weyl semimetals by dichroic photoemission*, Phys. Rev. Lett. **129**, 246404 (2022).

[54] J. Erhardt, C. Schmitt, P. Eck, M. Schmitt, P. Keßler, K. Lee, T. Kim, C. Cacho, I. Cojocariu, D. Baranowski, V. Feyer, L. Veyrat, G. Sangiovanni, R. Claessen, and S. Moser, *Bias-free access to orbital angular momentum in two-dimensional quantum materials*, Phys. Rev. Lett. **132**, 196401 (2024).

[55] Q. Wu, A. A. Soluyanov, and T. Bzdušek, *Non-Abelian band topology in noninteracting metals*, Science **365**, 1273 (2019).

[56] G. Kresse and J. Furthmüller, *Efficient iterative schemes for ab initio total-energy calculations using a plane-wave basis set*, Phys. Rev. B **54**, 11169 (1996).

[57] G. Kresse and D. Joubert, *From ultrasoft pseudopotentials to the projector augmented-wave method*, Phys. Rev. B **59**, 1758 (1999).

[58] P. E. Blöchl, *Projector augmented-wave method*, Phys. Rev. B **50**, 17953 (1994).

[59] J. P. Perdew, K. Burke, and M. Ernzerhof, *Generalized gradient approximation made simple*, Phys. Rev. Lett. **77**, 3865 (1996).

[60] S. Steiner, S. Khmelevskyi, M. Marsmann, and G. Kresse, *Calculation of the magnetic anisotropy with projected-augmented-wave methodology and the case study of disordered* $Fe_{1-x}Co_x$ *alloys*, Phys. Rev. B **93**, 224425 (2016).

[61] A. A. Mostofi, J. R. Yates, Y.-S. Lee, I. Souza, D. Vanderbilt, and N. Marzari, *wannier90: A tool for obtaining maximally-localised Wannier functions*, Comput. Phys. Commun. **178**, 685 (2008).